Rotordynamic Instability Control For Floating-Ring Bearing Supported Turbo-Shaft By Angled Oil-Injection Feedholes

Daniel Tamunodukobipi, Yong Bok Lee

Abstract— **Rotordynamic instability is a performance defect common with floating-ring bearing (FRB) supported turbo-shaft. Contemporary solutions are hinged on structural modifications, which technology is saturated. Alternatively, this work presents the test-results for the effects of different feed-angles ($\Phi=0°-60°$) on FRB rotordynamic stability behaviors across 6.0−30 krpm. The results indicate that the whirl frequency, orbit-size and sub-synchronous amplitudes are mitigated, particularly for large injection-angles. The pockets of pressure along the circumference minimize the asymmetries of pressure-fields, reduce destabilizing forces and enhance damping. However, supply-pressure must be optimized higher back-pressure at feedholes' exits. Thus, it is concluded that angled-feedhole significantly improves FRB rotordynamic stability in high-performance turbo-systems.**

Index Terms— **Floating-ring bearing; dynamic coefficients; analytical modeling; oil-bearing.**

I. INTRODUCTION

Fluid-film journal bearings (JBs) in machinery applications are needed to: provide support for the shaft; ensure good damping for shock-loads; isolate vibration; minimize instabilities; provide effective cooling; and reduce noise [1]. The characteristics of these JBs contrast widely, particularly in their rotordynamic stability, load capacities, damping properties, and thermo-hydrodynamic behaviors [2]. Hence, bearing practitioners are constantly confronted by the needs to optimize bearing designs, by utilizing various structural relations for improved stability performance and energy efficiencies for their rotor-bearing units [3]. Fundamentally, the strive is aimed at producing high load capacity and dynamically more stable support bearings that can guarantee in machines a good functional performance, durable service life, low friction loss, and enhanced rotordynamic stability[2-4].

These desirable characteristics are exhibited in different combinations by the various JBS. Comparatively, floating-ring bearing (FRB) has shown excellent rotordynamic stability and thermal control in applications involving light-load, high-speed turbomachinery. In turbochargers, FRB provides effective convective cooling to minimize thermal effects, and excellent damping to attenuate undesirable lateral vibrations as the turbo-rotor traverses the different critical speeds of its operating speed range [2, 4-10]. Figure 1 presents the descriptive schematics of FRB.
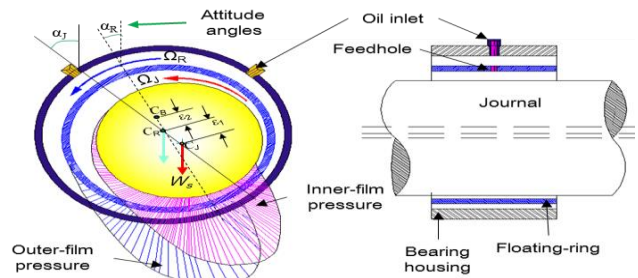
Daniel Tamunodukobipi, Department of Marine Engineering, Rivers State University, Port Harcourt, Nigeria, +2347087643334.
Yong Bok Lee, Center of Urban Energy System Research, Korea Institute of Science and Technology, Songbuk-gu, Seoul, Korea

Fig. 1 Description of a floating-ring bearing and the 2 film pressure distributions

Research Scope and Method

This work describes the experiment procedure and presents the test-data for the effects of implementing angled oil-injection feedholes on the rotordynamic stability and load capacity of the mid-span grooved *FRB*. The oil is injected in direction opposed to the journal rotation to retard the inner-film tangential velocity. The reduced inner-film velocity minimizes the cross-coupled stiffness coefficients; and hence improves rotordynamic stability. The inclination of the 6 identical feedholes to the radius of the floating-ring is varied from $\Phi=$ 0°, 30°, 45° to 60°. The experiment is conducted on a specialized *FRB*-dynamic-test rig equipped with seasoned instrumentation for reliable and repeatable data acquisition. The rotordynamic performance assessment is based on the measured whirl frequencies, orbit sizes and sub-sync motion amplitudes for the different feed-angles

II. PREVIOUS CONTRIBUTIONS

Bearing-based rotordynamic instability has been tackled assiduously by researchers using various structural models [2, 3, and 5]. Despite imbalance, rotordynamic instability has been identified as a fundamental source of turbo-shaft vibration and performance irregularities [4-7]. As solution-finding, Tanaka and Hori [2] consider the implications of changes in bearing geometry for a TC rotor, and present stability charts for different clearance ratios. Their analysis indicates that for $C_2/C_1 \leq 1.6$: the rotor-bearing system is unstable at low speeds, becomes stable at moderately high speeds, and finally unstable at very high speeds. This unique behavior is experimentally confirmed by Tatara [9]. Subsequently Tanaka et al. [10, 11] proposed stability-criteria which indicate that the speed range of stable operation of an *FRB*-supported rotor can be extended by increasing the C_2/C_1 and R_2/R_1, while the supply-pressure (P_s) and slenderness (L/D) are simultaneously reduced. However, reducing (P_s, L/D) or enlarging (C_2/C_1) is constrained by the tradeoff on the load capacity. Nonetheless, the analysis of Tanaka and the test-data of Tatara are remarkable because

they demonstrate the occurrence of multiple but discrete instability speed-ranges: low- and high-speed instabilities, and a middle-speed stable region.

Unfortunately, the resizing of bearing dimensions for better rotordynamic stability is counter-effective and limited in many cases because of the machines' technical constraints. A journal bearing is an integral component of a machine; and it must be designed to match compatibility in size, shape, position and functionality with other associating components. Thus, to attenuate bearing-based rotordynamic instability without violating structural constraints, Tondle [12] and San Andrés and Childs [13] evolve and apply the concept of angled oil-injection for the single-film journal bearing (SFJB). The researchers demonstrate that implementing an appropriate oil-injection angle is effective for instability control. Correspondingly, Chow [3] employs helical grooved ring-journal arrangement to facilitate the inner-film flow. The analysis shows that the pumping effect of the helical groove, in spite of boosting the cooling flow, also enhances FRB stability behavior by mitigating cross-coupled forces and providing higher damping.

References [3, 12, and 13] highlight the dependency of FRB rotordynamic stability on the fluid-flow interaction with film-pressures, and its import on the bearing dynamic force parameters. Figure 2 displays FRB signal waterfall showing sub-sync instability.
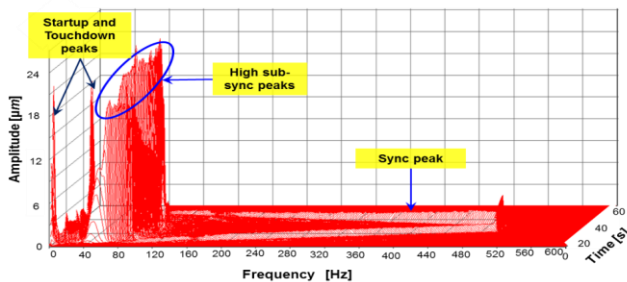

Fig. 2 FRB signal waterfall for speed-up-and-down test indicating massive sub-sync peaks

Obviously, contemporary studies on FRB rotordynamic stability are more concerned about the structural dimensions than fluid flow redirection [5-9]. However, the technology in this area is overly saturated and in dire need of innovation. More so, some of the structural changes outlined by Tanaka [2, 10] and Born [5], to extend the frequency range of FRB stability are adverse to load capacity and thermo-hydrodynamic performance of the bearing. In addition, machine structure (shape and size) cannot be altered arbitrarily because a smaller or bigger bearing of improved stability is required for the shaft. The only window of opportunity resides in regulating the fluid-flow. On this premise, this work harnesses its relevance and explores the rotordynamic implications of redirecting oil injection-angle. Note that the bearing based rotordynamic instability prevails within certain speed ranges, and is responsible for violent vibration and performance ineffectiveness, particularly in turbocharger (TC) [8-11].

III.   THEORY OF SWIRL-CONTROL MECHANISM BY ANGLED OIL-INJECTION

Figure 3 shows a schematic of the angled oil-injection feedholes. The current concept for *FRB* rotordynamic instability control involves changing the fluid flow direction by using angled oil-injection feedholes on the floating-ring to slow down the inner-film tangential velocity.
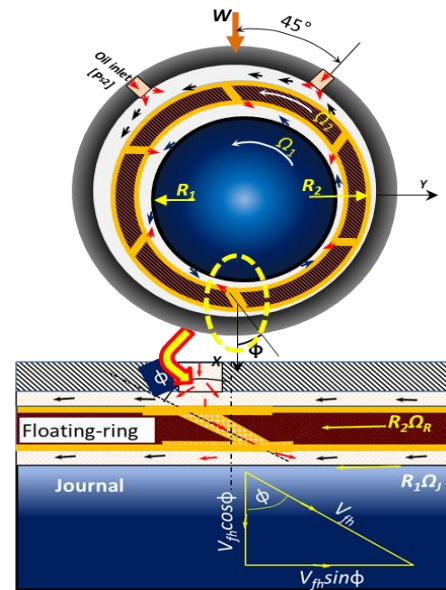

Fig. 3 Schematic of *FRB* anti-swirl oil-injection mechanism and its velocity triangle

The momentum interaction of the injected oil impinging upstream against the inner-film generates a localized pressure rise within the inner groove. These pockets of pressure fields retard the tangential flow velocity and improve the symmetry of the circumferential film-pressure distribution. Consequently, the cross-coupling forces are reduced. A lower cross-coupled stiffness reflects invariably as an attenuated whirl frequency ratio (WFR). At low WFR, the FRB supported rotor is more stable.

IV.   FRB LINEARIZED DYNAMIC FORCE PARAMETERS IDENTIFIER (*LDFPI*)

FRB rotordynamic stability characterization without a companion test-data validation is merely academic. Regrettably, *FRB* dynamic force parameters are uncommon because of its experimental challenges [14]. The response signals are impaired by sub-synchronous peaks, imbalance response and electro-mechanical noise. Therefore, test based linearized force coefficients identification is classified as almost unfeasible [14, 15]. This supposition is valid only where frequency-bandwidth selection and data coherency are neglected. Thus, Tamunodukobipi, et al. [17] develop the linearized dynamic force parameter identification program for characterizing FRB; and also present the resulting test data. Excerpts from their identified FRB dynamic force coefficients are provided in the Appendix and used in this study to facilitate understanding of FRB dynamic behavior.

A.   Derivation of LDFPI

Define the impedance matrix as $D_{(\omega)} = \left[K - \omega^2 M + i\omega C \right]$. Then, import the recorded response functions matrix [$\underline{H}_{(\omega)}$] from the FFT-analyzer onto the processor and transform it into an impedance matrix [$\underline{D}_{(\omega)}$] by taking the inverse at each j-frequency point.

$$\begin{bmatrix} D_{XX} & D_{XY} \\ D_{YX} & D_{YY} \end{bmatrix}_j = \frac{\begin{bmatrix} H_{YY} & -H_{XY} \\ -H_{YX} & H_{XX} \end{bmatrix}_{j=n1:\delta:n2}}{(H_{XX}H_{YY} - H_{XY}H_{YX})} \quad (1)$$

The sub-matrix $\left(D_{j(\omega)}\right)$ computed for each chosen j^{th} frequency is a 2-by-2 linearly independent complex impedance matrix, which is stacked to form the global impedance matrix $\left\lfloor\underline{\underline{\underline{D}}}_{(\omega)}\right\rfloor$. The global matrix $\left\lfloor\underline{\underline{\underline{D}}}_{(\omega)}\right\rfloor$ is decomposed into the constituent real, $\mathsf{Re}\left[\underline{\underline{\underline{D}}}_{(\omega)}\right]$, and imaginary, $\mathsf{Im}\left\lfloor\underline{\underline{\underline{D}}}_{(\omega)}\right\rfloor$, arrays as given in equations (3). Note that the triple-underscore symbolizes a stack.

$$\begin{bmatrix} \underline{\underline{\underline{D}}}_{XX} & \underline{\underline{\underline{D}}}_{XY} \\ \underline{\underline{\underline{D}}}_{YX} & \underline{\underline{\underline{D}}}_{YY} \end{bmatrix} = \left\{ \begin{array}{cc} \left(D_{XX(\omega)}\right)_{(j=n1)} & \left(D_{XY(\omega)}\right)_{(j=n1)} \\ \left(D_{XX(\omega)}\right)_{(j=n1+\delta)} & \left(D_{XY(\omega)}\right)_{(j=n1+\delta)} \\ \vdots & \vdots \\ \vdots & \vdots \\ \left(D_{XX(\omega)}\right)_{(j=n2)} & \left(D_{XY(\omega)}\right)_{(j=n2)} \\ \left(D_{YX(\omega)}\right)_{(j=n1)} & \left(D_{YY(\omega)}\right)_{(j=n1)} \\ \left(D_{YX(\omega)}\right)_{(j=n1+\delta)} & \left(D_{YY(\omega)}\right)_{(j=n1+\delta)} \\ \vdots & \vdots \\ \vdots & \vdots \\ \left(D_{YX(\omega)}\right)_{(j=n2)} & \left(D_{YY(\omega)}\right)_{(j=n2)} \end{array} \right\} \quad (2)$$

$$\left. \begin{array}{l} \mathsf{Re}\left[\underline{\underline{\underline{D}}}_{j(\omega)}\right] = \mathsf{Re}\begin{bmatrix} \underline{\underline{\underline{D}}}_{XX} & \underline{\underline{\underline{D}}}_{XY} \\ \underline{\underline{\underline{D}}}_{YX} & \underline{\underline{\underline{D}}}_{YY} \end{bmatrix}_{j=n1:\delta:n2} \\ \\ \mathsf{Im}\left[\underline{\underline{\underline{D}}}_{j(\omega)}\right] = \mathsf{Im}\begin{bmatrix} \underline{\underline{\underline{D}}}_{XX} & \underline{\underline{\underline{D}}}_{XY} \\ \underline{\underline{\underline{D}}}_{YX} & \underline{\underline{\underline{D}}}_{YY} \end{bmatrix}_{j=n1:\delta:n2} \end{array} \right\} \quad (3)$$

Plotting the real and the imaginary arrays of equations (3) is important to unveil the intrinsic linear and non-linear spectra of the measured signals. At this instance a correct frequency bandwidth selection can be made. Figure 4 shows the low and high cut-off limits for parameters identification and the consequence of excessive use of filter. By equating separately the real and imaginary parts of the impedance matrix, we have two sets of linearly independent equations:

$$\mathsf{Re}\left(\underline{\underline{\underline{D}}}_{(\omega)} = K - \omega^2 M\right) \text{ and } \mathsf{Im}\left(\underline{\underline{\underline{D}}}_{(\omega)} = \omega C\right).$$

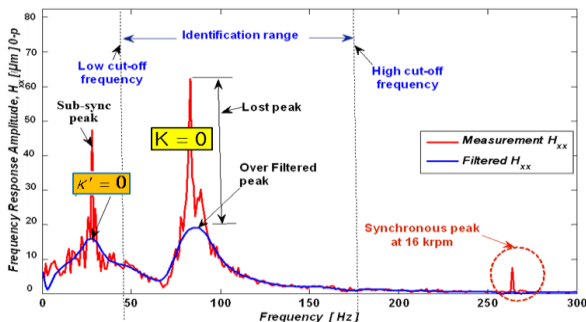These relations are translated into 2 sets of characteristic lines as defined by equations (4).

Fig. 4 Frequency range for FRB force parameters identification

$$\left. \begin{array}{l} \mathsf{Re}\left(\widetilde{D}_{(\omega)}\right) = \widetilde{K} + Q\widetilde{M} \\ \mathsf{Im}\left(\widetilde{D}_{(\omega)}\right) = \kappa' + \omega\widetilde{C} \end{array} \right\} where: \begin{array}{l} Q = -\omega^2 \\ \kappa' = const. \end{array} \quad (4)$$

Then, the least-square regression solutions are applied to generate the curve-fitting line coefficients $\left(\widetilde{M}, \widetilde{K}, \widetilde{C}, \kappa'\right)$, which are related to the force coefficients as: $\left(M = \widetilde{M}\right)$, $\left(K = \widetilde{K}\right)$ and $\left(C = \kappa'\!\!\big/\!\omega + \widetilde{C}\right)$. The coefficient ($\kappa'$) is usually neglected because it has no technical relevance. Nonetheless, if (K and κ') have opposite signs, the signal curve will exhibit double peaks occurring, respectively, at ($K=0$) and ($\kappa' = 0$) as indicated by Figure 4. The relation for FRB equivalent dynamic force coefficients are succinctly represented by equation (5); while the curve-fitting data [$\widetilde{H}_{(\omega)}$] for the transfer functions is obtainable using equation (6). The first subscript is the direction of impact force, while the second indicates the direction of displacement. Figure 5 presents the program implementation flow-chart.

$$\begin{bmatrix} \widetilde{D}_{XX} & \widetilde{D}_{XY} \\ \widetilde{D}_{YX} & \widetilde{D}_{YY} \end{bmatrix} = \\ \begin{bmatrix} K_{XX} - \omega^2 M_{XX} + i\omega C_{XX} & K_{XY} - \omega^2 M_{XY} + i\omega C_{XY} \\ K_{YX} - \omega^2 M_{YX} + i\omega C_{YX} & K_{YY} - \omega^2 M_{YY} + i\omega C_{YY} \end{bmatrix} \quad (5)$$

$$\begin{bmatrix} \widetilde{H}_{xx} & \widetilde{H}_{xy} \\ \widetilde{H}_{yx} & \widetilde{H}_{yy} \end{bmatrix}_j = \left(\frac{\begin{bmatrix} \widetilde{D}_{yy} & -\widetilde{D}_{yx} \\ -\widetilde{D}_{yx} & \widetilde{D}_{xx} \end{bmatrix}}{\widetilde{D}_{xx}\widetilde{D}_{yy} - \widetilde{D}_{xy}\widetilde{D}_{yx}} \right)_j ; j = n_1 : \delta : n_2 \quad (6)$$
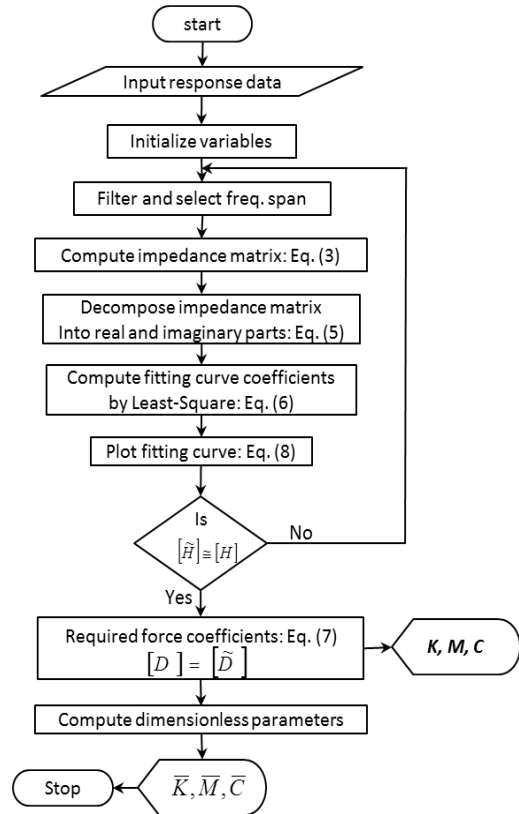

Fig. 5 Flow-chat for LS based force parameters identification programs

B.   Reliability Assessment of LDFPI−Model against Data by Instrumental Variable Filter (IVF) and Real -Time Measurement

Having identified the force coefficients, the performance of LDFPI is evaluated against the measured response data and the curve-fitting data of the instrumental variable filter (IVF), as indicated in Figure 6. The *IVF* generates a badly skewed curve-fitting with force coefficients that are largely inconsistent. The poor curve-fitting is caused by its iterative procedure which muddles up the response signals to generate their distorted hybrids. Conversely, the well-chosen frequency span of the *LDFPI* algorithm produces good curve-fitting and reliable test results. The *LDFPI* is definitive on convergence and preservative of the response signals' unique properties. Each frequency impedance matrix is considered as linearly independent of any other, and its coefficients are uniquely characterized. Therefore, the developed model is valid and more effective than IVF for characterizing FRBs.
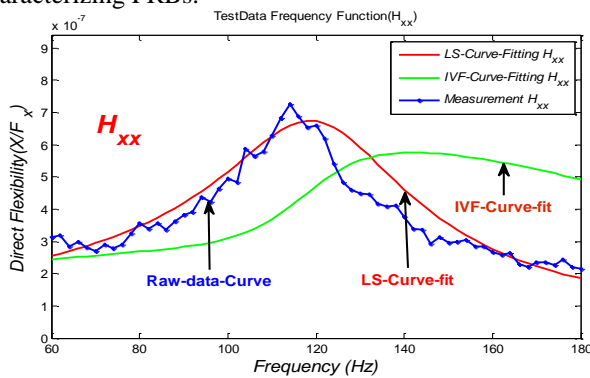

**Fig. 6 Comparison of curve-fittings of FRB response data by LDFPI and IVF methods**

V.   DESCRIPTION OF FRB ROTORDYNAMIC TEST-RIG

Figures 7 and 8 present the descriptive images of the test rig and the shaft, respectively, while Tables 1 and 2 provide information on the test-facility specifications and the predicted mode shapes. The experiment rig consists of a central FRB housing, with a length of 61.0 mm, inner diameter of 42.0 mm and outer diameter of 100.0 mm, suspended by eight support springs ($Ks = 2.0\times10^3 N/m$). Four pairs of adjustable, sliding-contact axial pins projected from the bearing pedestals serve as pitch-stabilizers. At mid-span of the bearing housing a pair of *x* and *y* directed load-platforms takes the impact loads. The vertical load-platform also has a provision for the static load, which is linked to a load-cell via a cable-and-spring conjunction. Two pairs of gap sensors attached orthogonally on the housing measure the floating-ring and the housing displacements. The Floating-ring speed and convective oil temperature are measured by a speed-tracking gap-sensor and a thermocouple installed axially on the ring-retainer plate.

The test shaft is SCM440, with a mass of 0.948 kg, length of 314.00 mm, and diameter of 24.00 mm, which runs through the floating-ring and is supported at both ends by twin tandem angular-contact ball bearings in the end-pedestals.   An inverter-controlled motor with maximum power of 75 kW at a spin-speed of 60 krpm drives the rigid shaft via a spline-coupling. Table 2 speed conversion: 100 Hz = 6.0 krpm.
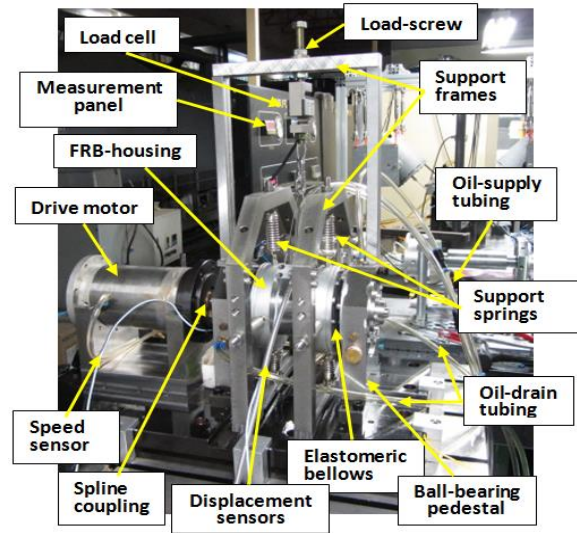
(a) Pictorial image of test-rig
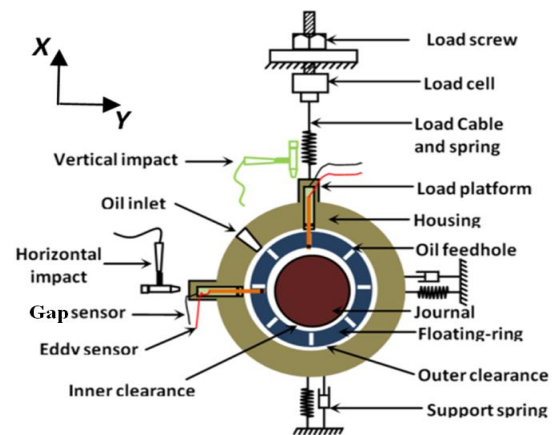
(b) Schematic representation

Fig. 7 Descriptive sectioned view of FRB rotordynamic test-rig (image and schematic)

Table I: Test facility dimensions and sensors

Parameter	Value
Floating-ring and journal dimensions	
Inner radial clearance, C_1, [μm]	50
Outer radial clearance, C_1, [μm]	75
Radius ratio of ring, R_2 / R_1	1.75
Groove width , b, [mm]	3.0
Length of ring , L=(L_T - b)/2, [mm]	21
Slenderness ratio, $L/2R_2$	0.5
Oil feedhole diameter, [mm]	2.8
Number of oil feedholes]	6
Mass of ring, [kg]	0.15
Mass of housing, [kg]	4.06
Specific constants	
Ring thermal expansion [μm/m-ºC]	18.4
Journal thermal expansion [μm/m-ºC]	17.2
Density of oil,[kg/m³]	862
Viscosity of oil at 40°C [cSt]	32.1
Sensor specifications	
U8-Gap senor sensitivity [V/mm]	7.87
U8-Gap senor resolution [kHz]	70
U8-Gap senor range [mm]	0.35~2.0
U8-Gap senor temp. drift [% F.S/°C]	± 0.004

Table II: Predicted mode shapes of shaft

Mode	Speed. (Hertz)	X direction	Y direction	Z direction
Conical	1,020.7	4.6539e-005	1.0063	4.2679e-26
1st bending	1,900.1	0.0046344	0.00010693	4.5868e-22
2nd bending	4,780.5	4.3242e-006	5.165e-006	1.0711e-08
3rd bending	6,7283.1	5.1877e-006	4.3081e-006	9.6715e-11
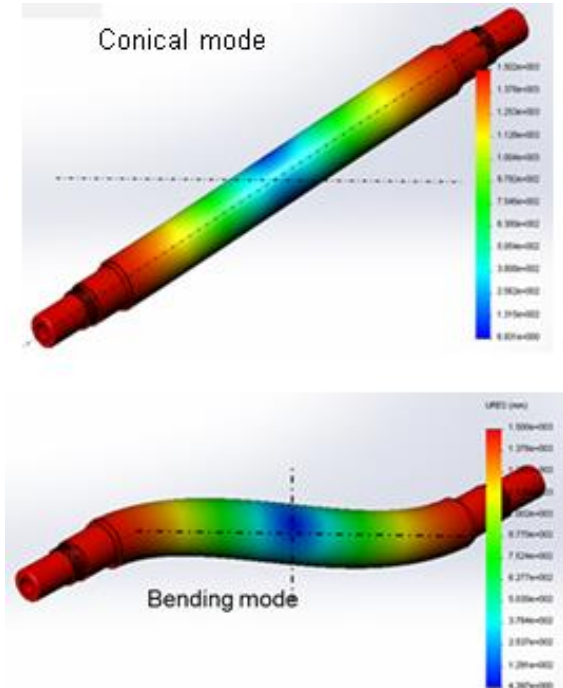
Fig. 8 Representation of structural rotor and the predicted free-free mode shapes

Test Procedure for Parameters Identification

The test apparatus is assembled with no floating-ring, lubricant and rotation; and tested for the baseline data. This data (of the support-springs) will be subtracted from the actual test-data. Removal of the floating-ring prevents any possible interference from the ring. The test is repeated with the floating-ring inserted, and the specific load of 50 k*N/m²* and the supply pressure of 0.2 *MPa* are being imposed. Response data from impact-test are recorded at 2.0 *krpm* interval over a speed range of 6.0 ~ 30 *krpm*. In this test the overall force coefficients of the *FRB* are evaluated from the response data of the housing relative to the journal. The remaining 2 pairs of gap sensors capture data used for the whirl orbits and amplitudes.

During the measurement for the whirl orbits, both static and impact loadings are removed while oil supply temperature and pressure kept constant. The inlet oil-temperature is maintained at 28.5 $^\circ C$. Signal orbits and sub-sync motion amplitudes are recorded on the FFT-analyzer for each feed-angle. Two oil supply-pressures (P_S= 0.2 and 0.3 MPa) are investigated and the average of 3 repeated measurements are plotted for each case.

VI. TEST-DATA FOR EQUIVALENT STIFFNESS COEFFICIENTS OF FRBs

Figure 9 shows the equivalent force coefficients computed for Φ = 0° and 60°, using Lund [18] as given in equation (7). The

force coefficients for calculating K_{eq} are excerpts from Ref. [17] as given in the Appendix. The results indicate that the equivalent stiffness (K_{eq}) of the normal injection is slightly higher than that of the angled injection FRB. However, this difference becomes progressively smaller as the journal speed is being raised. Ultimately at Ω_J> 26 krpm, the Keq for Φ= 60° surpasses that of the normal injection. The initially low K_{eq} for Φ= 60° is due to a lower inner film pressure.

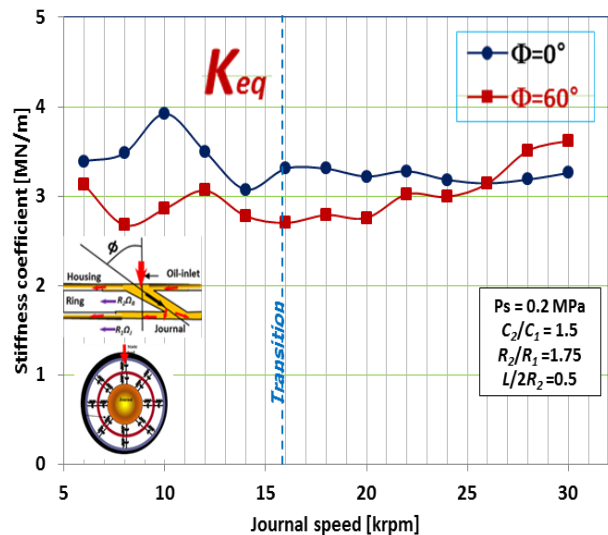$$K_{eq} = \frac{K_{xx}C_{yy} + K_{yy}C_{xx} - K_{xy}C_{yx} - K_{yx}C_{xy}}{C_{xx} + C_{yy}} \quad (7)$$

Fig. 9 *FRB* equivalent non-dimensional stiffness coefficients for Φ= 0°, 60°

This discrepancy in load capacity is given 2 physical explanations. Firstly, the feedhole length is longer for Φ= 60° by a factor of secant (60°), which implies higher viscous friction, and hence higher pressure drop within the duct of the feedhole for fresh oil charge. Secondly, the counter-flow injection is resisted by the inner-film tangential flow. The resulting momentum exchange causes a build-up of back-pressure at the feedhole exit. This higher back-pressure further diminishes the inner-film supply. However, at elevated speed (>26 krpm), the viscous pressure drop in the feedhole is insignificant due to thermo-viscous reduction, and the back-pressure is over-shadowed by the centrifugal effect. Consequently, both FRBs' inner-films are vaporous and exhibit very similar pressure fields. Thus, their load capacities are barely the same.

A. Effect of Oil-Injection Angle on FRB-Supported Rotor's Signal Orbits

The sub-sync and sync signal amplitudes are visual indicators of the strengths of the bearing based instability and its corresponding imbalance response, respectively, [17]. Figure 10 compares the measured signal orbits for Φ= 0°, 30°, 45° and 60°. The data is recorded under a zero static-load. The signal orbit produced by the normal (Φ= 0°) injection is the largest. The orbit size diminishes with the increase in oil-injection angle. The whirl orbit for 60° injection is the least and is about 10% the size of 0° injection. The smaller the orbit, the lesser the rotor is displaced from the bearing axis.
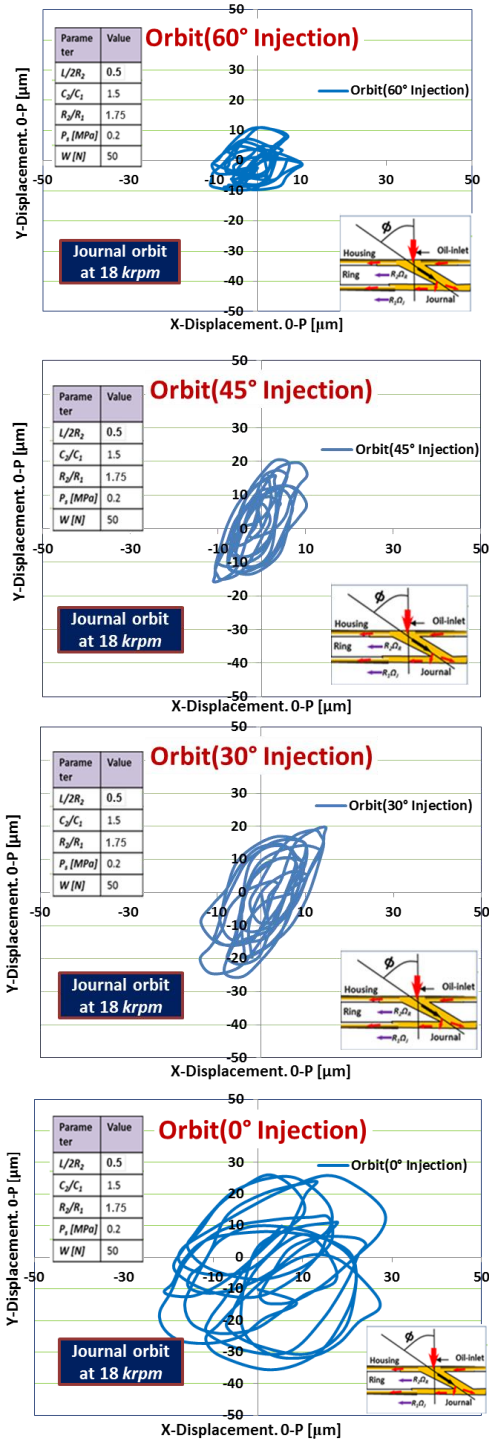
Fig. 10 Comparison of FRB-supported rotor whirl orbits for different oil-injection angles

A small whirl orbit implies reduced instability and lateral vibration. The 60° FRB is conspicuously the smallest and undoubtedly the most effective in mitigating rotordynamic instability.

B. Effect of Oil-Injection Angle on FRB Sub-Sync Signal Amplitudes

Figure 11 displaces sub-sync amplitudes of the different oil-injection angles for supply pressures of 0.2 MPa. The sub-sync curve produced by the normal (Φ= 0°) injection is the largest and has a maximum value of 74.16 μm, whereas the sub-sync curve for Φ=60° is 71.28 μm. At the transition speed (16 krpm): the normal injection has 68.36 μm as against 9.72

μm of 60° injection. Furthermore, the transition speed for angled injection FRB is earlier than the conventional FRB. This suggests that the middle-speed stable region, Ref. [2], is extended by implementing the anti-swirl injection feedholes. The inspection of the sub-sync curves of the different feed-angles indicates that the larger the oil-injection angle the smaller the sub-sync amplitudes. Such reduction depicts improved rotordynamic stability performance of FRB. This corroborates well the substantial shrinkage of the whirl orbit for larger Φ. The observed phenomenal reduction in the sub-sync amplitude (for Φ=60°) is ascribed to the improved symmetry of film pressure fields, larger damping and the relatively lower cross-coupled stiffness, as indicated in the Appendix.
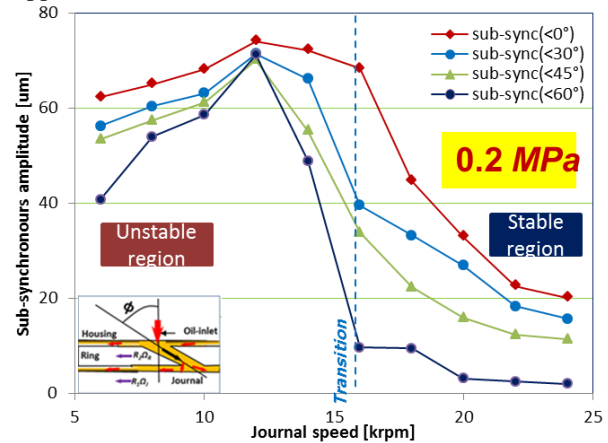

Fig. 11 Comparison of FRB-supported rotor sub-syncs for different oil-injection angles

C. Oil-Injection Angle, Supply Pressure and Rotordynamic Stability

Figure 12 presents the sub-sync amplitudes of the different oil-injection angles for supply pressures of 0.3 MPa. By raising the supply pressure to 0.3 MPa, the performance of the anti-swirl injection is enhanced. It is evidently so because the strength of the anti-swirl oil-injection to enforce symmetry of hydrodynamic pressure field becomes stronger. That is, the injected-oil tangential component ($V_\Phi = V_{fh} \sin\Phi$) of Figure 3 grows in intensity against the inner-film tangential flow. The resulting localized pressure fields which are evenly distributed along the circumferential groove are strong enough to compensate for the asymmetry of the inner-film hydrodynamic support. This minimizes the destabilizing forces and consequently reduces the sub-sync amplitude.
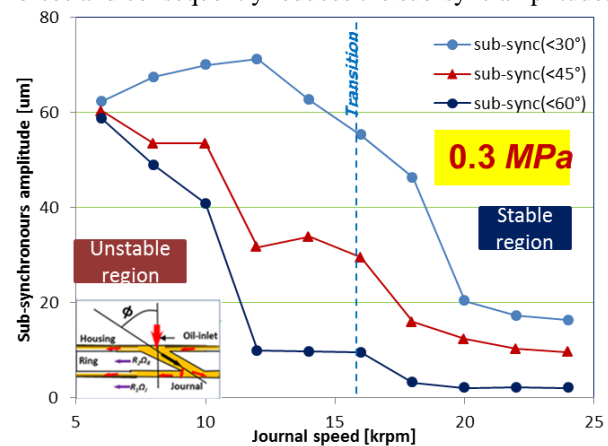

Fig. 12 Comparison of FRB-supported rotor sub-syncs for different oil-injection angles

However, Φ=30°-feed-angle FRB stability deteriorates because the contribution of ($V_Φ=V_{fh}\sinΦ$) to enforce symmetry is weaker than the radial component ($V_R=V_{fh}\cosΦ$). It is observed that radial component (V_R) aggravates pressure asymmetry, especially at large supply pressures. Thus, the whirl orbit for Φ=0° exhibits excessive boundary inference at low speeds. Thus, it is not represented in Figure 12.

However, it is observed that the Φ= 0° sync is lowest, while Φ= 60° sync is the largest. The larger the injection angle the more restricted the oil-supply to the inner-film. An insufficient supply pressure induces a starved inner-film and invigorates boundary lubrication. Hence the imbalance response becomes higher. Observably, the rise in the synchronous component is marginal within the test range (6 – 30 krpm), but could be significant for high-speed (>100 krpm) operations. Therefore, to ensure optimum stability performance, the swirl-control feed-angle should be matched for both the oil supply pressure and the system operating speed.

D. Swirl-Control Angle, Whirl Frequency Ratio and Stability

Figure 13 presents the whirl frequency ratios (*WFR*s), computed from Lund [18] as defined by equation (8). The *WFR* is larger for normal injection, which indicates higher propensity to rotordynamic instability. In contrast, the lower *WFR* of Φ= 60° implies a more stable FRB. This result is in agreement with the measurements in Figures 10 to 13. The WFRs of Φ= 30° and 45° are not given because their data almost overlap that of Φ= 0°.

$$WFR = \sqrt{\frac{(K_{eq} - K_{xx})(K_{eq} - K_{yy}) - Kx_yK_{yx}}{(C_{xx}C_{yy} - C_{xy}C_{yx})Ω^2}} \quad (8)$$
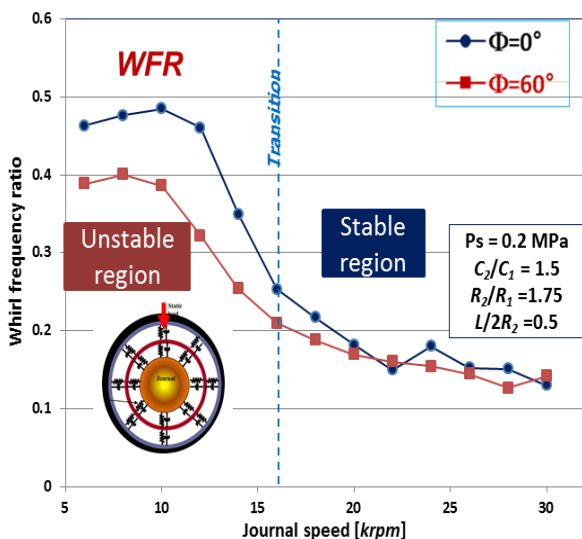

Fig. 13 Impact of varied *OISCM* angles and WFR curves

The results indicate that incorporating angled oil-injection in FRBs effectively minimizes self-excited sub-sync motions and considerably improves rotordynamic stability performance of their turbo-shafts. Optimum result is achievable only where the feed-angle is matched for both the supply pressure and journal speed.

VII. CONCLUSION

An experimental investigation of the rotordynamic stability behavior of floating-ring bearing (FRB), for different oil-injection angles (Φ=0°, 30°, 45°, 60°) and over a journal-speed range (6.0 ~ 30 *krpm*), is conducted and the results are presented. The test is performed for mid-span grooved FRB with dimensions ($R_2/R_1 = 1.75$, $L/D_2= 0.5$ and $C_2/C_1 = 1.5$). It is found that implementing angled feedhole *FRB*s significantly improves the rotordynamic stability performance of FRB-supported rotor. The whirl frequency, orbit and sub-synchronous motion amplitudes are considerably minimized, especially for large oil-injection angles. The flow-momentum interaction and the subsequent build-up of localized back pressures along the circumferential groove of the angled FRB improve the symmetry of hydrodynamic pressure forces which minimizes the destabilizing effects. The impacts of reduced cross-coupled stiffness and high damping are responsible for the observed stability improvement. Nonetheless, this advantage is constrained by the tradeoff on the inner-film lubricity which could induce boundary lubrication and consequently increase imbalance response: if an adequate oil supply-pressure is not sustained. Also, a starved FRB induces pulsation in turbocharger air-supply. Therefore, it is concluded that for optimal rotordynamic stability performance, the oil-injection angle should be selected to satisfy both the oil-supply pressure and the design operating speeds.

REFERENCES

[1] Malcolm E. and Leader, P.E., "Understanding Journal Bearings," Applied Machinery Dynamics Co., RotorBearingDynamics.com, Durango, Colorado, available: MLeader@RotorBearingDynamics.com

[2] Tanaka, M., and Hori, Y., 1972, "Stability Characteristics of Floating Bush Bearings," ASME J. Lubr. Technol., 94, pp. 248–259

[3] Chow, C.Y., 1983, "Dynamic Characteristics and Stability of a Helical Grooved Floating-Ring Bearing Operated in Turbulent Regime," ASLE Trans., **27**(2), 154-63

[4] Zeidan, F. Y. and Herbage, B.S., 1991, "Fluid film bearing fundamentals and failure analysis," Proc. 20th Turbomachinery symposium, pp. 161-186

[5] Born, H., 1987, "Analytical and Experimental Investigation of the Stability of the Rotor-Bearing System of a New Small Turbocharger," ASME Paper No. 87-GT-110

[6] Holt, C., San Andrés, L., Sahay, S., Tang, P., LaRue, G., and Gjika, K., 2003, "Test response of a turbocharger supported on floating ring bearings–part II: Comparisons to non-linear rotordynamic predictions," ASME Paper No. DETC 2003/VIB-48419

[7] Holt, C., San Andrés, L., Sahay, S., Tang, P., LaRue, G., and Gjika, K., 2005, "Test Response and Nonlinear Analysis of a Turbocharger Supported on Floating Ring Bearings," ASME J. Vibr. Acoustic., **127**, pp. 1–9

[8] Schweitzer, B., 2009, "Total instability of turbocharger rotors — Physical explanation of the dynamic failure of rotors with full-floating ring bearings," Journal of Sound and Vibration, doi:10.1016/j.jsv.2009.03.028

[9] Tatara, A., 1970, "An Experimental Study on the Stabilizing Effect of Floating Bush Journal Bearings," Bull. JSME, 13, pp. 859–863.

[10] Tanaka, M., Hori, Y., and Nasuda, T., 1975, ''A Theoretical Stability Analysis of Floating Bush Journal Bearing,'' ~in Japanese!,

Proceedings of the Japan Society of Mechanical Engineers, **750**, No. 6, pp. 153–156

[11] Tanaka, M., 1996, "A Theoretical Analysis of Stability Characteristics of High Speed Floating Bush Bearings," *Proceedings of the 6th International Conference on Vibrations in Rotating Machinery*, IMechE Conf. Trans. London, Paper C500/087/96, pp. 133–142

[12] Tondle, A., 1967, "Bearings with a Tangential Gas Supply," Gas Bearing Symposium, University of Southampton, Dept. of Mech. Engrg

[13] San Andrés, L., and Childs, D., 1996, "Angled Injection- Hydrostatic Bearings Analysis and Comparison to Test Results," ASME, Journal of Tribology.-290

[14] Tian, L., Wang, W.J., and Peng, Z.J., 2011, "Dynamic behaviors of a full floating ring bearing supported turbocharger rotor with engine excitation," Journal of Sound and Vibration doi:10.1016/j.jsv.2011.04.031

[15] San Andrés, and Kerth, J., 2004, "Thermal Effects on the Performance of Floating Ring Bearings for Turbochargers," Proceedings of the Institution of Mechanical Engineers, Part J: J. Engineering Tribology, **218**, pp. 1-14

Daniel Tamunodukobipi, PhD, MNSE, Lecturer, Rivers State University, Port Harcourt, Nigeria.

Yong Bok Lee, Professor, Center of Urban Energy System Research, Korea Institute of Science & Technology, Songbuk-gu, Seoul, Korea.